IOPscience iopscience.iop.org

Home Search Collections Journals About Contact us My IOPscience

Comparison of the performance of the next generation of optical interferometers

This content has been downloaded from IOPscience. Please scroll down to see the full text.

2012 Metrologia 49 455

(http://iopscience.iop.org/0026-1394/49/4/455)

View the table of contents for this issue, or go to the journal homepage for more

Download details:

IP Address: 194.117.40.96
This content was downloaded on 22/09/2015 at 12:15

Please note that terms and conditions apply.

IOP Publishing — Metrologia
Metrologia **49** (2012) 455–467 — doi:10.1088/0026-1394/49/4/455

Comparison of the performance of the next generation of optical interferometers

Marco Pisani[1], Andrew Yacoot[2], Petr Balling[3], Nicola Bancone[1], Cengiz Birlikseven[4], Mehmet Çelik[4], Jens Flügge[5], Ramiz Hamid[4], Paul Köchert[5], Petr Kren[3], Ulrich Kuetgens[5], Antti Lassila[6], Gian Bartolo Picotto[1], Ersoy Şahin[4], Jeremias Seppä[6], Matthew Tedaldi[2] and Christoph Weichert[5]

[1] Istituto Nazionale di Ricerca Metrologica (INRIM), Torino, Italy
[2] National Physical Laboratory (NPL), Hampton Road, Teddington, Middlesex, TW11 0LW, UK
[3] Czech Metrology Institute (CMI), Prague, Czech Republic
[4] TÜBİTAK, Ulusal Metroloji Enstitüsü (UME), PO 54, 41470 Gebze–Kocaeli, Turkey
[5] Physikalisch-Technische Bundesanstalt (PTB), D-38116 Braunschweig, Germany
[6] Centre for Metrology and Accreditation (MIKES), PO box 9, Fi-02151 Espoo, Finland

E-mail: Andrew.yacoot@npl.co.uk

Received 24 November 2011, in final form 6 April 2012
Published 23 May 2012
Online at stacks.iop.org/Met/49/455

Abstract
Six European National Measurement Institutes (NMIs) have joined forces within the European Metrology Research Programme funded project NANOTRACE to develop the next generation of optical interferometers having a target uncertainty of 10 pm. These are needed for NMIs to provide improved traceable dimensional metrology that can be disseminated to the wider nanotechnology community, thereby supporting the growth in nanotechnology. Several approaches were followed in order to develop the interferometers. This paper briefly describes the different interferometers developed by the various partners and presents the results of a comparison of performance of the optical interferometers using an x-ray interferometer to generate traceable reference displacements.

(Some figures may appear in colour only in the online journal)

1. Introduction

Dimensional measurements play a crucial role in almost every aspect of modern life and are essential at the nanometre and sub-nanometre level for the semiconductor industry and more broadly to support the growth and development of nanotechnologies. For any measurement to have meaning it needs to be traceable to its fundamental unit of measurement; in the case of dimensional metrology this unit is the metre. The usual route for traceability to the metre is via optical interferometry using the wavelength of a helium–neon laser, either stabilized (Quinn 2003) or unstabilized (Stone *et al* 2009). The recent survey of nanometrology in Europe (Leach *et al* 2011) highlighted the requirement for better displacement metrology including more accurate optical interferometry to support European nanotechnology. This is in keeping with the recommendations of the International Technology Roadmap for Semiconductors (ITRS) of 2009 which states that 'Metrology methods must routinely measure near, and at, atomic scale dimensions' and that from 2015 dual pattern technology requires an image placement accuracy below 1 nm. Applications requiring better metrology include precise positioning for semiconductor manufacturing, EUV-lithography, surface science metrology and process control in nanofabrication. Laser interferometers provide the metrology for pattern placement measurements on photomasks and for position control in wafer scanners. The use of double patterning techniques has particularly high-accuracy demands: for mask metrology tools, a reproducibility of about 0.3 nm (3σ) is currently demanded. Within the National Metrology Institutes (NMIs) effort has also been directed towards developing metrological atomic force microscopes (AFMs) to provide a means of traceably calibrating transfer standards for scanning probe microscopy. The traceability of

 © 2012 BIPM & IOP Publishing Ltd

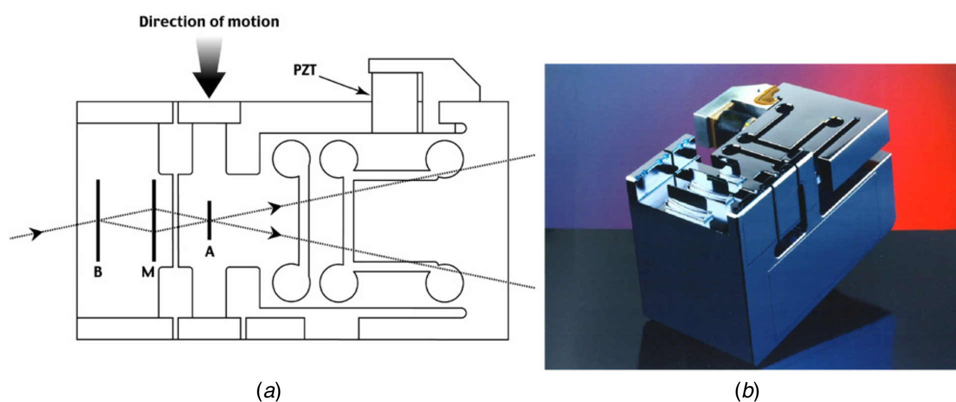

(*a*) (*b*)

Figure 1. Schematic plan view (*a*) and photograph (*b*) of the monolithic XRI.

metrological AFMs is derived from optical interferometers that provide traceability for the scanning axes of the microscope (Danzebrink *et al* 2006). The AFMs have atomic resolution, but this is an order of magnitude better than most optical interferometers. Although atomic steps have been imaged using the interferometer signal from a metrological AFM (Yacoot *et al* 2007), there is a clear need for an improvement in optical interferometry resolution and accuracy if it is going to be used for picometre metrology, i.e. sub-nanometre length measurements or measurements with sub-nanometre uncertainty. To achieve this, interferometer optical and electronic non-linearities, noise and stability well below 0.1 nm are necessary. Over the years there has been considerable effort directed towards designing interferometers with sub-nanometre non-linearity (Bobroff 1993, Lawall and Kessler 2000, Peggs and Yacoot 2002, Hou *et al* 2009). The NANOTRACE project funded by the European Metrology Research Programme has developed and tested several new interferometry techniques to achieve a target accuracy of the interferometers of 10 pm. Several promising techniques have been developed that will be applicable in different situations. The non-linearity of these interferometers designed within the project has been traceably measured by comparing the displacements measured by the optical interferometers against a displacement generated by an x-ray interferometer (XRI).

2. X-ray interferometry

Before describing the optical interferometers, the XRI is introduced. X-ray interferometry was first demonstrated by Bonse and Hart (1965a, 1965b), and a few years later Hart (1968) showed that an XRI could be used for metrology. It can be regarded as a ruler or translation stage where the graduations or steps are based on the lattice spacing of silicon. Unlike most optical interferometers, the fringe spacing in an XRI is independent of the wavelength of the incident radiation; it is determined by the spacing of diffraction planes in the crystal from which x-rays are diffracted: in this case the (2 2 0) planes of silicon with a spacing of 0.192 015 497 nm $\pm 1.2 \times 10^{-8}$ nm, at 22.5 °C and a pressure of 1 atm. Silicon is the material normally used for an XRI since it is readily available in a pure, defect-free form with a known crystallographic orientation and lattice parameter (Windisch and Becker 1990, Martin *et al* 1998, Mohr *et al* 2008, Massa *et al* 2009, Andreas *et al* 2011). The fringe spacing in an XRI is therefore not only several orders of magnitude smaller than that in an optical interferometer, thereby obviating the need for fringe division as with optical interferometry, but it is also traceable.

Figures 1(*a*) and (*b*) show a schematic diagram and photograph of the monolithic XRI developed for the combined optical and XRI project (COXI) (Basile *et al* 2000) and used in this comparison. It is made from a single crystal of silicon in which three thin, vertical, equally spaced lamellae were machined. A flexure stage that has a range of 10 µm and is driven by a piezoelectric transducer (PZT) has been machined around the third lamella. X-rays are incident on the first lamella (B) and are diffracted from the (2 2 0) planes. Two diffracted beams are produced; the first lamella can be thought of being analogous to the beamsplitter in an optical interferometer. The two beams diffracted from the first lamella are incident on the second lamella (M). Two more pairs of diffracted beams are produced and one beam from each pair converges on the third lamella (A). These two beams give rise to a fringe pattern whose period is equal to that of the lattice planes from which the x-rays were diffracted. The fringe pattern would be too small to resolve individual fringes; however, when the third lamella is translated (by the PZT) parallel to the other two lamellae, a moiré fringe pattern between the coincident beams and the third lamella is produced with a period of 0.192 nm. Consequently, the intensity of the beams transmitted through the third lamella varies sinusoidally as the third lamella is translated with respect to the first two lamellae. By measuring the intensity of one of these transmitted beams it is possible to measure the displacement of the third lamella. Since the displacements are traceable, the XRI can be regarded as a ruler with sub-nanometre divisions. At the sides of the interferometer, there are three optical mirrors allowing the XRI to be coupled to an optical interferometer. These mirror surfaces were coated with aluminium to increase their reflectivity.

By servo-controlling the (PZT) used to move the third lamella it is possible to either hold the third lamella in a fixed position or move it in discrete steps equal to one x-ray fringe period (Bergamin *et al* 1997). A comparison of the results obtained by the optical interferometer with the displacement of the XRI yields the non-linearity in the optical interferometer. The non-linearity of an NPL-designed plane mirror differential

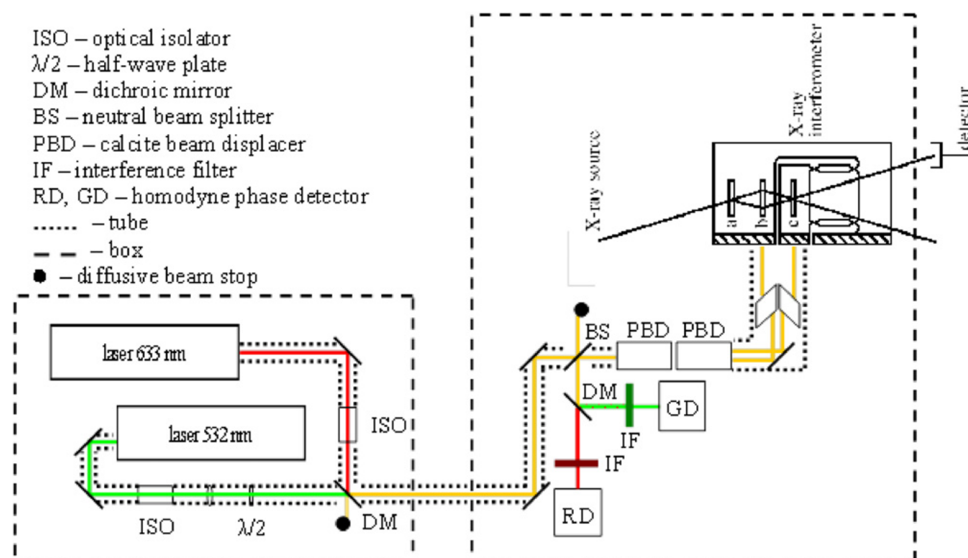

Figure 2. Block diagram of the two-wavelength common-path interferometer with the XRI.

interferometer and a Heidenhain linear encoder have both previously been measured using x-ray interferometry (Yacoot and Downs 2000, Yacoot and Cross 2003). In both cases cyclic errors with amplitudes of much less than 100 pm were observed once the Heydemann correction had been applied (Heydemann 1981, Birch 1990).

The platform and the control system developed for the XRI are described in detail in Yacoot and Kuetgens (2012). The XRI was mounted on a breadboard made from the low expansion alloy Invar™ that was rotated to align the XRI to the incoming x-rays. The interferometer and breadboard were enclosed in a lead-lined wooden box to provide both thermal and radiation shielding. Insulating foam was placed around the box and as many heat sources as possible were removed from the room. All control electronics and computers were placed in an adjacent control room. The temperature stability inside the wooden lead-lined box was a few millikelvin over the duration of the measurement, which typically lasted less than 1 h.

3. Interferometers

3.1. The two-wavelength common-path homodyne interferometer (CMI)

The setup of a two-wavelength common-path interferometer shown in figure 2 was first described by Křen and Balling (2009). The main reason for using two independent homodyne interferometers with different wavelengths is ability to resolve non-linearities with different periods. The He–Ne laser (model Renishaw XL-80, 633 nm) and frequency-doubled Nd : YAG laser (model Prometheus 20, 532 nm) emit beams with a sufficient relative optical frequency and power stability (transferred to change of measured path difference) so that they can be combined and overlapped using a dichroic mirror (DM). This two-wavelength beam is transmitted through an optical window into the separate box containing the XRI. Although the interferometer arms were the components most sensitive to external disturbances, the laser pointing stability in front of a beam splitter (BS) was kept as stable as possible.

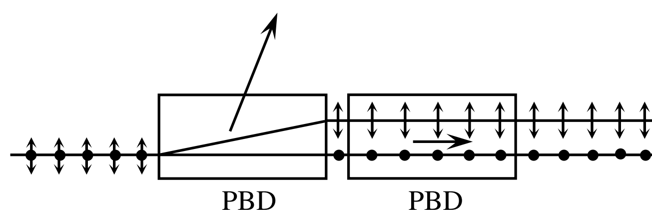

Figure 3. The polarization separation in two calcite PBDs.

The combined beams pass through a 50 : 50 BS and orthogonal polarizations of both wavelengths are split into interferometer arms using the refractive properties of the calcite polarizing beam displacers (PBDs) by means of refractions in the birefringent crystals (figure 3). These two PBDs have optical axes perpendicular to each other to compensate for the optical path difference in the interferometer arms. The total beam separation obtained by PBDs is 6 mm. When two thick Brewster windows (each in a different interferometer arm) are added, the total beam separation exceeds 14 mm (to match the separation between XRI lamellae). Thus the optical path difference between the interferometer arms is rigid and matched as far as possible to avoid unwanted drifts and vibrations. Another feature of the interferometer design is the suppression of parasitic beams from unwanted reflections: the slight tilting of optical elements to remove unwanted back reflections and the high optical grade calcite PBDs (with extinction ratio better than 100 000 : 1) are used for a parasitic signal removal.

The orthogonally polarized reflected beams were recombined by the PBDs and deflected by the BS. The second DM separated the beams of different wavelength and band-pass interference filters (IFs) remove unwanted residual optical radiation of the wrong wavelength in both arms to avoid optical crosstalk. The interferometer phase shifts were measured by

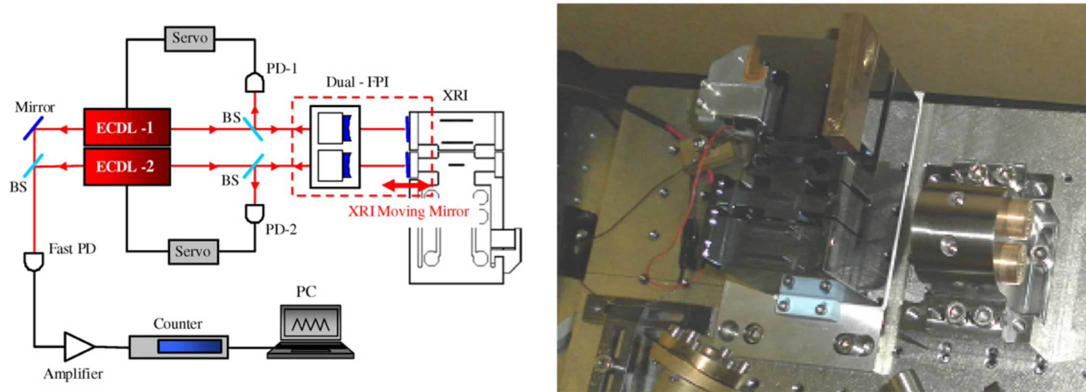

Figure 4. (*a*) Block diagram of the apparatus used for the differential Fabry–Perot (UME)–XRI comparison and (*b*) photo of the FPI against the XRI.

homodyne detectors (RD, GD; model Blata MLS R4.3) with built-in polarization decoding. Output signals were collected by analogue-to-digital converters (model TiePie HS4 with effective 14-bit signal-to-noise ratio and suitable low electric crosstalk) and acquired by a computer program calculating elliptic corrected positions. The measured displacements were also corrected for the effects of ambient air refractive index calculated in real time using data from a calibrated weather sensor system that measured temperature, pressure and humidity.

3.2. Differential Fabry–Perot interferometer (UME)

Investigation of non-contact small displacement measurements using Fabry–Perot interferometers (FPIs) and diode laser frequency shift techniques was demonstrated by Gamidov *et al* (1996) and Roos *et al* (1996). Precision displacement measurements (up to 300 µm with nanometre accuracy) based on beat frequency measurements using FPI and two He–Ne lasers were realized by Haitjema *et al* (2000). However, the narrow tuning range of the He–Ne laser necessitates the locking and unlocking of the laser in order to extend the measurement range up to 300 µm. This can be overcome by direct laser frequency measurements of compact external cavity diode lasers (ECDLs) that have a larger mode-hop free tunable range (>100 GHz). The accuracy of Fabry–Perot displacement measurements over a macroscopic range (50 mm) with sub-picometre uncertainty has been described by Durand *et al* (2011) as an extension of the work by Lawall (2005). The application of a differential (dual channel) FPI system will decrease the environmental effects by at least one or more orders of magnitude (Bitou 2009) and is also suited to cases where it is impossible to apply active temperature and vacuum control. A block diagram and a photo of the experimental setup for the differential FPI–XRI comparison are shown in figures 4(*a*) and (*b*).

Displacement measurements of the moving mirror of the XRI were performed using a dual channel FPI and two frequency-stabilized ECDLs. Each cavity of the FPI comprised a spherical mirror together with an aluminium coated plane surface on the XRI. The radius of curvature of the mirrors was 75 mm and reflectivity of the spherical mirrors was 98.96% at 780 nm. Owing to the lower reflectivity of the aluminium coated plane surface, the finesse value for the observed reflection resonances of the FPI was about 15. The Super Invar ™ block designed for holding the spherical mirrors (right-hand side of photograph in figure 4(*b*)) had adjustments for setting the distance between these mirrors and the two aluminium coated mirrors on the XRI (figure 4). In order to decrease the effects of temperature and refractive index fluctuations, an additional enclosure was placed around the cavity air path.

The frequencies of the ECDL-1 and ECDL-2 were stabilized electronically on the reference channel and tracking channel of the dual FPI using the detected reflection resonances on PD-1 and PD-2, respectively. In addition, parts of the laser beams were superimposed on a fast photodetector (>10 GHz) and the frequency of the amplified beat signal between the two lasers was measured by a computer-controlled counter. Displacement of the mirror of the XRI changed the cavity length of the tracking channel of the dual FPI. This change induced a frequency change of ECDL-2 which was stabilized on cavity length of the tracking channel. Finally, by measuring the frequency change between the two lasers, the displacement of the XRI was analysed. For the control of the wavelengths, both lasers were tuned to Rb D_2 absorption lines (780.24 nm).

3.3. Electro-opto-modulator linearized heterodyne interferometer (INRIM)

A double-pass (1 fringe = 158 nm) heterodyne interferometer using a red He–Ne laser in a differential optical configuration was constructed. The interferometer employs common-path parallel output beam optics mounted on a circular Invar™ plate. Tip-tilt and vertical adjustments of the interferometer plate were realized by three Invar™ screws 120° apart on kinematic supports (figure 5(*a*)). The half- and quarter-wave plates were mounted on rotators. A polarizing beam splitter (PBS) separates the two polarizations (components) of the incident beam, which are then fed to the reference and moving mirrors. A rotation mechanism, integrated in the plate support, allows for fine alignments of the PBS. The laser provides two orthogonally polarized components separated in frequency by approximately 3.5 MHz. A small

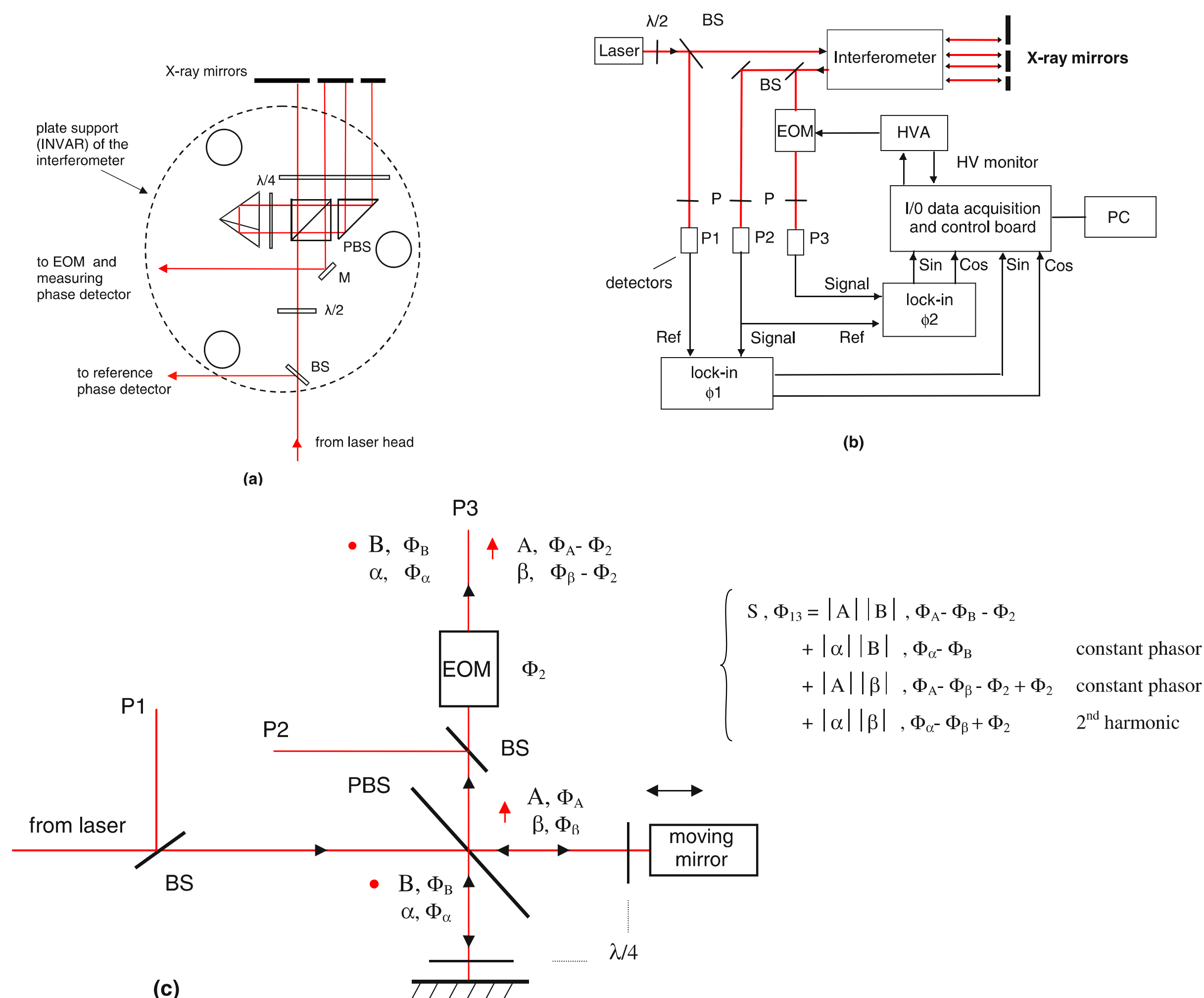

Figure 5. Block diagram of INRIM optical interferometer (*a*), electronics (*b*) and operating principle (*c*).

component of these beams is extracted for use as a reference signal prior to light entering the interferometer. The beam at the output of the interferometer is divided by a BS: one beam is sent to a transverse electro-optic modulator (EOM), which is aligned with the slow and fast axes that are aligned to the polarizations of the two beam frequency components; the other beam is measured using a photodiode whose output is sent to a lock-in amplifier. By means of two separate receivers, the heterodyne beat signal is detected before and after the EOM. Two high-frequency lock-in amplifiers (SRS844) are used to measure the phase of the interferometer. Lock-in 1 measures ϕ_1, the phase difference between the reference signal and the output of the interferometer. Lock-in 2 measures the phase difference between the interferometer output and the interferometer output signal once it has passed through the EOM. The phase added by the EOM is proportional to the voltage supplied by a high-voltage amplifier (HVA). Using a LabVIEW based control system the total phase ($\phi_1 + \phi_2$) of the interferometer is zeroed at the start of each measurement of a sub-wavelength displacement. With the slow and fast axes oriented to the polarizations of the two beam frequency components, the EOM acts only on the phase of components along the slow axis. Assuming that no constant phasor terms are added by the EOM ($\phi_2 = 0$ at $V_{\mathrm{EOM}} = 0$ or $V_{\mathrm{EOM}} = V_{\mathrm{o}}$; V_{o} initial offset) the total phase is zeroed by adding a phase ϕ_2 which corresponds to the actual phase of the interferometer. The operating principle is outlined in figure 5(*c*) using a phasor representation of the main components of the heterodyne signal (S, ϕ_{13}), whose phase corresponds to the sum of the phases ϕ_1 and ϕ_2. The use of two lock-ins measuring ϕ_1 and ϕ_2 instead of a single lock-in for the total phase enables counting of the number of fringes and direct monitoring of the phase across the EOM. Detection systems based on fundamental and harmonics of the heterodyne signals were used in the comparison measurements.

3.4. Separated beams heterodyne interferometer (PTB)

This interferometer, which is shown in figure 6, was designed to minimize interpolation non-linearities commonly associated with frequency mixing in heterodyne interferometers (Bobroff 1993). The proposed design avoids this effect by illuminating the interferometer with light from a frequency-doubled Nd : Yag laser ($\lambda = 532$ nm) fed from two separate fibres. This ensures that each arm of the interferometer only contains components with the correct frequency unlike an interferometer that relies on polarization components for splitting the input beam (Tanaka *et al* 1989). Naturally, there

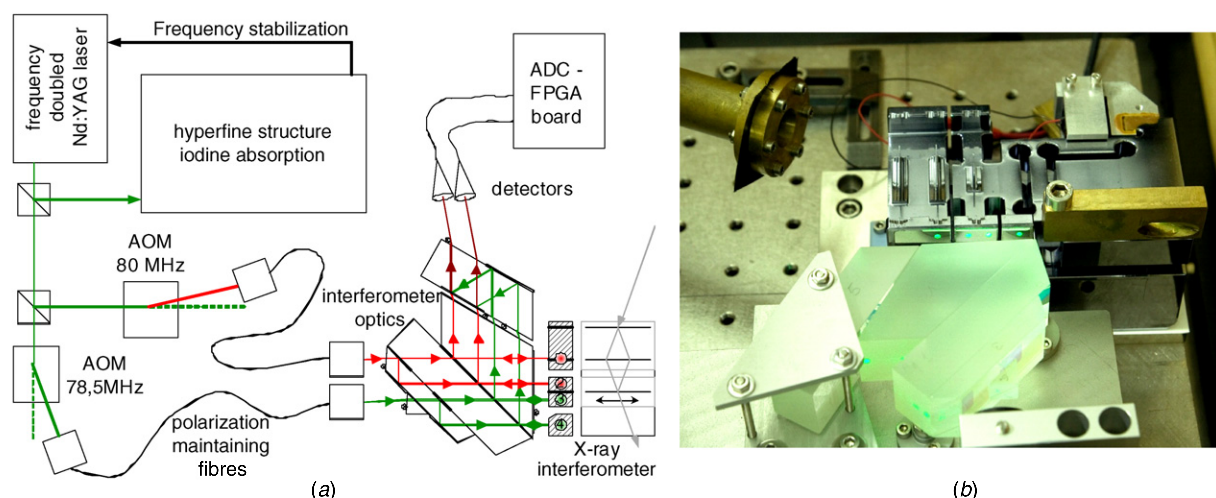

Figure 6. (*a*) Block diagram of the PTB separated beams heterodyne interferometer and (*b*) configuration in front of the XRI.

may be some stray light with the wrong polarization in each arm of the interferometer; however, its contribution is very small. The two incoming beams with respective frequencies f_1 and f_2 are split into two parallel beams at the first plane parallel plate using a non-polarizing BS and a mirror. All beams pass through a PBS on the second plate. One beam of each frequency is reflected by the moving mirror and the other one by the reference mirror. After the reflection all beams pass through a quarter-wave plate again and are then reflected at the PBS. The beams with different frequencies interfere with each other after passing a plane parallel plate whose thickness is different from that of the first BS plate. The interferometer is highly symmetric with respect to glass and air paths and also compensates for angular motion between the interferometer optics and the XRI. A glass prism is used to minimize the air path; however, this is at the cost of higher sensitivity to temperature gradients within the glass.

In heterodyne systems the displacement information is contained in ac waveforms that are insensitive to dc changes in signal levels. In addition perturbations close to the beat frequency, e.g. due to fibre movement, can be prevented using an appropriate beat frequency. The comparison measurements with the XRI have been carried out with a beat frequency of 1.5 MHz generated by two acoustic opto-modulators (AOM) operating at frequencies near 80 MHz.

The laser interferometer signals were analysed using an analogue-to-digital converter card manufactured by Struck Innovative Systeme. It came with eight 16 bit input channels having a sampling rate up to 100 MHz. Two ADCs are combined with one field programmable gate array (FPGA) which executes a user-defined program for the implementation of a lock-in algorithm for the evaluation of phase between measurement and reference signal. The lock-in algorithm, implemented in the programming language VHDL, was able to work at the full ADC input speed of 100 MHz. The AD-converted input signals were mixed down and a low-pass filter was applied to these measurements on consecutive windows of 2048 values. Using this approach a continuous data transfer rate of 48.8 kHz has been used, which is suitable for dynamic control applications.

3.5. Non-linearity correction using a capacitive sensor (MIKES)

The initial MIKES configuration has been described in detail by Seppä *et al* (2011). The aim was to develop a cost-effective but accurate solution for elimination of the periodic non-linearity of interferometers. The setup for the comparison described here differs slightly from the original. A more advanced frequency counter with improved sample rate and time resolution (Agilent 53230A) was used. In addition, the main components of the interferometer were tightly integrated into an Invar™ block inside an enclosure. The main design targets were a stable construction with low thermal expansion and having a minimized measurement arm and dead path lengths.

The interferometer system uses a 633 nm He–Ne laser head, a single-pass differential optical arrangement with symmetrical reference and measurement beam paths and a capacitive position sensor. The measurement setup with the XRI is shown schematically in figure 7. Before the comparison measurement with the XRI, the interferometer periodic non-linearity was measured and corrected using the capacitive sensor. The periodic correction method with a capacitive sensor was developed earlier at MIKES by Korpelainen *et al* (2010), although it has subsequently been improved with a new mathematical model and different hardware (Seppä *et al* 2011). Using this method it is possible to linearize the interferometer and compensate for the drift of the non-linearity parameters by frequent or continuous measurement of the correction. The laser is a commercial frequency-stabilized heterodyne laser with an internal acousto-optic modulator-based frequency split. The two orthogonally, linearly polarized optical frequencies of the output beam are set 20 MHz apart by the AOM.

The simple single-pass design has symmetrical optical paths to both photodetectors; the interferometer generates the reference beat frequency signal with the same optical components as the measurement signal. The construction improved the stability of the interferometer signal by reducing high-frequency phase noise by a factor of 10 over commercially

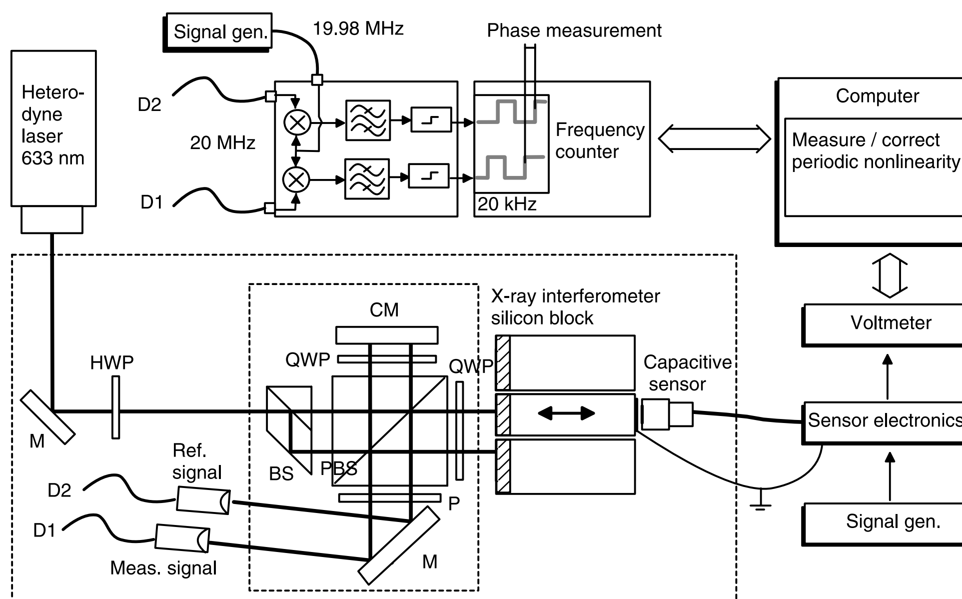

Figure 7. MIKES measurement setup with XRI. M: mirror, CM: common mirror, BS: (neutral) beamsplitter, PBS: polarizing beamsplitter, P: polarizer, QWP: quarter-wave plate, HWP: half-wave plate, D1 and D2 are detectors. The outer dashed line is the shielding box of the XRI. The inner dashed line is the shielding enclosure for the interferometer optics.

available double-pass interferometer optics with a separated reference signal. This improvement is likely to be due to reduced sensitivity to noise from the laser source, such as polarization, pointing and power instability.

The beam from the laser source travels via a mirror and a half-wave plate to a non-polarizing BS. The half-wave plate is used to adjust the planes of polarization of the two beams. The BS divides the beam into two parallel beams: one for reference and one for measurement. Both beams are split into two by the PBS so that ideally one frequency, with p-polarization, goes straight through the PBS and the other, with s-polarization, is reflected towards the mirror common to both beams. After recombining the polarizations and using a 45° tilted polarizer, length difference between beam paths of the interferometer arms is encoded into the phase difference of the two 20 MHz beat frequencies.

For the detection of the phase difference, the measurement and reference signals are mixed with a common 19.98 MHz signal to increase the frequency counter's phase resolution. After band-pass filtering with three cascaded first-order filters, the same phase difference exists between two 20 kHz signals. The signals are sharpened with comparators, after which the resulting square waves are fed to the frequency counter. The frequency counter time resolution of 20 ps corresponds to a displacement resolution of 0.13 pm. This is more than sufficient to detect the phase difference with high precision, and the limiting factor is the residual noise from the mixers after band-pass filtering. The fringe subdivision noise is approximately 1/10 000, or 40 pm, without averaging, at a maximum sample rate of 7 kHz.

The capacitive sensing system, developed at INRIM (Nerino *et al* 1997), had a grounded reference. The (second) mirror surface of the moving part of the XRI (on the opposite side) was gold coated and electrically connected to the ground of the capacitive sensor electronics. The capacitive sensor was approximately 20 µm away from the grounded gold mirror. The electronics were fed with a stable ac voltage signal of 60 kHz from a signal generator. The ac output voltage from the sensor electronics to the voltmeter is proportional to the displacement, i.e. the inverse of the capacitance.

The correction of periodic non-linearity error was made by first measuring the capacitive and interferometric position synchronously, scanning over several optical interferometer fringes, and fitting the periodic non-linearity model to the data. Then the interferometer measurement was made using the previously obtained periodic correction for the interferometer phase. Using a separate reference for linearization allowed for compensation of all sources of periodic error.

4. Comparison results

For all of the comparisons, the optical interferometer under test was aligned to the XRI which was stepped through a displacement corresponding to several optical fringes in steps of individual x-ray fringes. At each x-ray fringe position the position as measured by the optical interferometer was recorded. The displacement measured by the optical interferometer was then compared with the displacement generated by the XRI and the difference revealed the non-linearity in the optical interferometer.

Although each comparison measurement was performed using the same XRI under the same operating conditions, the data acquisition systems used for the various optical interferometers were different, as were the data sampling rates. For this reason it is not realistic to compare noise levels and the performance of each system and to tabulate the results. Each comparison measurement against the XRI represents a stand-alone traceable characterization of the non-linearity of the system under examination, highlighting performance and

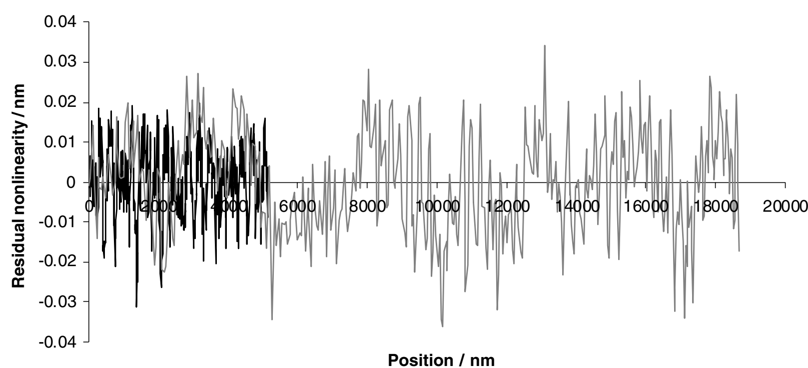

Figure 8. Examples of residual non-linearity errors for optical interferometer settings in CMI (up to 20 µm range with Nano-OP100 stage, grey line) and in NPL with XRI stage (5 µm range, black line) with scanning speed close to 1 $\mu m\,s^{-1}$ (0.1 s averages)

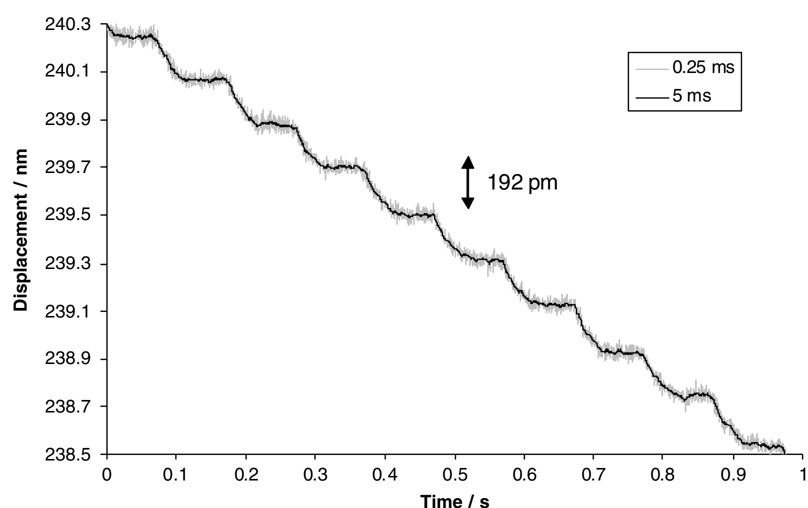

Figure 9. Example of steps measured by the optical interferometer when the XRI was stepping through individual x-ray fringes: grey line with averaging over 0.25 ms, black line with averaging over 5 ms.

critical aspects. For this reason the results of each system are presented and discussed separately.

4.1. The two-wavelength common-path homodyne interferometer (CMI)

The residual non-linearity of the individual optical interferometers operating at 633 nm and 532 nm can be determined by examining the different periodic errors measured by the two interferometers. When the optics of the interferometer are properly aligned, unwanted interference changes are suppressed. It was found that residual non-linearity below 10 pm is achievable (see figure 8). The amplitudes of non-linearity with fringe periodicity for both wavelengths 633 nm and 532 nm were found to be about 5 pm with the Nano-OP100 Invar™ stage in CMI and non-linearity amplitudes about 5 pm in average were obtained with standard deviations from 1 pm to 3 pm for measurements using the XRI stage (without silicon lattice stepping mode). The CMI optical interferometer measurements of XRI steps can be seen in figure 9. Each plateau of XRI steps was analysed after measurements and their deviations from linearity were calculated and are shown in figure 10. The standard deviations from a single scan are up to 10 pm. Nevertheless the statistical error of non-linearity is reduced down to 5 pm for the average of three consecutive scans. The amplitude of non-linearity with fringe period (corresponding to wavelength 633 nm) is only about 5 pm in each scan. Thus similar residual non-linearity of a step measurement was found (under the same adjustment) as the value obtained previously from a difference between 633 nm and 532 nm interferometers in faster and longer XRI scans without need of a silicon reference. Thus a non-linearity of the 633 nm interferometer was validated independently and can be determined against the 532 nm interferometer.

4.2. Differential Fabry–Perot interferometer (UME)

In the comparison between the differential FPI and the XRI, the main activities focused on determination of noise levels, investigation of influence of temperature drift in interferometers, investigation of non-linearity of the interferometers and measurement of displacements of more than two optical fringes of a $\lambda/4$ interferometer illuminated with a He–Ne laser, i.e. >316 nm. The experimental results for detection of one and a half fringes of XRI displacement are shown in figure 11. The frequencies of the reference laser (ECDL-1) and the tracking laser (ECDL-2) were stabilized on the lengths of the reference and the moving channels of the dual interferometer. The XRI moved one x-ray fringe forward,

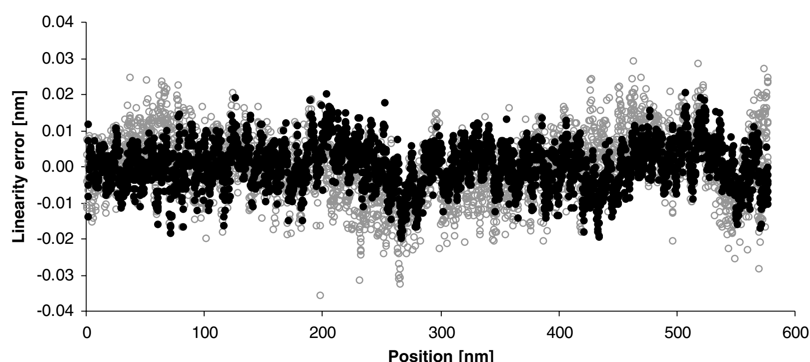

Figure 10. The 633 nm interferometer error from linear regression as a function of individual step position (a single scan (open circles) and an average of three values on each plateau from successive scans (filled)).

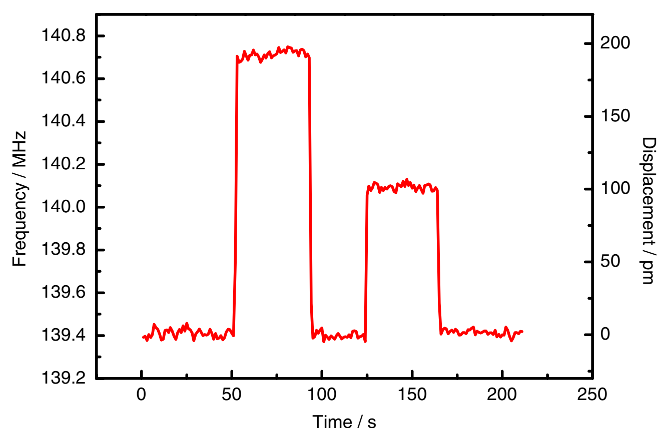

Figure 11. One and half fringe displacement of the XRI detected by laser beat frequency technique with the differential FPI.

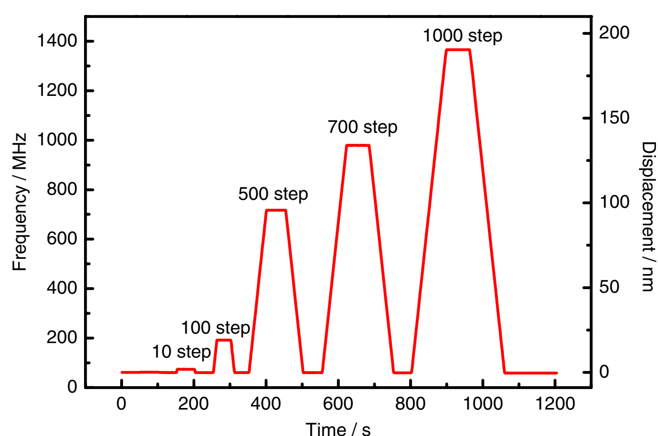

Figure 12. Graph showing displacements of XRI up to 1000 steps.

remained there for $\sim$50 s, returned to its initial position and after a few tens of seconds moved forward a half fringe. It stayed there for $\sim$50 s and returned to the initial position. Figure 11 shows the frequency changes in the Fabry–Perot system and corresponding displacement changes as a function of time. As can be seen from figure 11, one fringe movement of the XRI introduced a frequency change from 139.40 MHz to 140.71 MHz (Δbeat frequency $=$ 1.3 MHz) and a half fringe introduces a frequency change from 139.41 MHz to 140.09 MHz (Δbeat frequency $=$ 0.68 MHz).

Similar measurements were realized for 1, 10, 100, 500, 700 and 1000 steps of x-ray fringe movement (figure 12). During the movement of the XRI the laser beat frequency changed from 60.5 MHz to 1373.5 MHz. The sloping sides of the trapezoids in figure 12 are due to the 100 ms delay in each step. Analysis of the results in figure 12 showed that each x-ray fringe movement introduced an average frequency shift of 1313 kHz. In other words, 1000 step movement (192.0155 nm) of the XRI induced 1313 MHz laser frequency shift. The free spectral range (FSR) measurements were realized in order to determine the scaling between the frequency changes and length changes of FPI. To obtain the FSR for the channels of the interferometer, both lasers were locked to respective reflection resonances and the beat frequency was measured. The FSR of an FPI can be expressed by FSR $= c/2LN$ where c is the speed of light, L is the mirror spacing and N is the degeneration factor. $N = 1$ for a plane mirror FPI and $N = 2$ for a confocal interferometer where the mirror spacing L and the radius of curvature R of the mirror are equal. FSR of a non-confocal FPI with an adjustable mirror spacing may be expressed with higher ($N > 2$) degeneration factors (Kruk *et al* 2005, Budker *et al* 2000). During the comparison measurements, the high-resolution reflection resonances were obtained for a mirror spacing of approximately 56.2 mm. The measured FSR was 889.2 MHz, leading to $N = 3$. The frequency change of one FSR is observed for $\lambda/2$ and $\lambda/4$ cavity length changes for the plane mirror interferometer and the confocal interferometer, respectively. Similarly, frequency change of one FSR (889.2 MHz) for the non-confocal FPI arrangement used during these comparison measurements was observed for a $\lambda/6$ ($780.24/6 = 130.04$ nm) cavity length change. Thus, the displacement value obtained through FSR scale of FPI (889.2 MHz/130.04 nm) is comparable to the displacement value generated by the XRI (1313 MHz/192.0155 nm). In other words, the same ratio (1313 kHz/192 pm) for frequency shift to displacement was obtained.

The measurement for a displacement up to 345 nm (1800 fringes) is shown in figure 13. The XRI returns back to its initial position from a pre-aligned position that corresponds to 2363 MHz and again moves to that position from the initial position. The slight frequency difference corresponding to the pre-aligned position is due to temperature drift. A 1 µm measuring range is possible with the present system parameters.

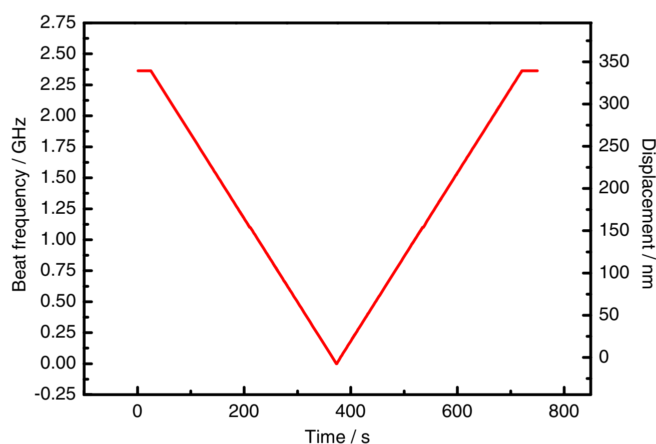

Figure 13. Displacement measurement of the XRI for a range up to 345 nm.

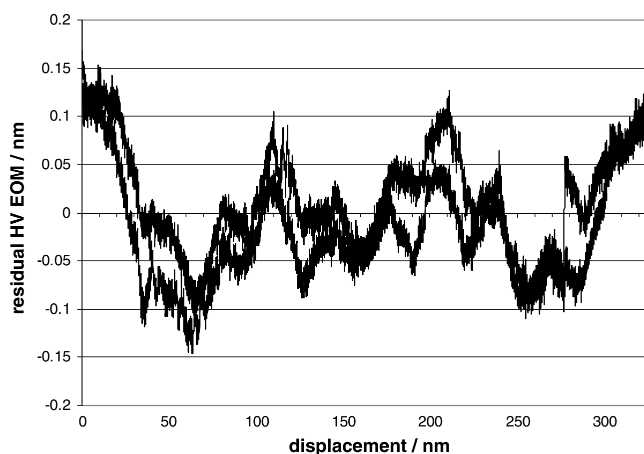

Figure 14. Residual non-linearity in INRIM interferometer (EOM linearized) from a bi-directional scan.

To assess the uncertainty due to the lasers, both lasers were locked to the Rb D_2 lines. A stability measurement for a time of more than 1 h showed that a peak-to-peak fluctuation of the frequency stability was below 10 kHz, which corresponds to a displacement value that is less than 1.5 pm.

The factor mostly affecting the uncertainty of the displacement measurements in this comparison was temperature drift and environmental fluctuations in the dual channel interferometer. To analyse the effect of temperature drift in the dual or single channel interferometer both lasers were locked to the length of channels of the dual interferometer or one of the lasers was locked to the Rb atomic transitions, respectively, and the frequency drift of the beat signal was measured. Over 1000 s, the temperature drift was 15 mK. During this time single and dual channel drifts of 7.3 nm and 0.1 nm were observed, respectively. By analysing this result and also by analysing the noise level fluctuation in figure 11, it is possible to conclude that the resolution for displacement measurements in the comparison using beat frequency techniques and dual channel interferometers is better than 2 pm. Finally, non-linearity measurements during the comparison show that the standard deviation of difference between the experimental data and the linear fit is less than 3 pm in the displacement range up to 345 nm (1800 fringes). Throughout the measurements with the XRI, laser frequencies were tuned to the Rb D_2 lines that correspond to wavelengths near 780.24 nm. Under this condition, a 1000 step displacement (192.0155 nm) of the XRI changed the laser frequency by approximately 1313 MHz and as a result this frequency tuning changed the wavelength of the laser by about 2.6 pm.

4.3. Electro-opto-modulator linearized heterodyne interferometer (INRIM)

The interferometer optics, the EOM and the three photodiodes with built-in preamplifiers were all mounted inside the thermal enclosure, whereas the laser beam was fed into the interferometer by an optical window in the enclosure. Scans of 1700 x-ray fringes equal to about the maximum OPD phase shift given by the EOM, i.e. two optical fringes of the double-pass interferometer, were performed in the comparison runs.

Possibly due to a poor alignment of the optics, specifically the quarter-wave plates and retroreflector, the phase of the double-pass interferometer showed a predominant periodicity of the residuals corresponding to half wavelength ($\lambda/2$), whereas the double-pass interferometer has a $\lambda/4$ OPD periodicity. Such a large non-linearity component is mainly from the unwanted mixture of the two beam polarizations in the second pass of the interferometer. In addition, the half wavelength ($\lambda/2$) components of the non-linearity were not compensated for by the EOM-driven phase shift. The uncorrected phase of the interferometer (ϕ_1), the phase across the EOM (ϕ_2) as well as the voltage applied to the EOM to zero the total phase ($\phi_1 + \phi_2$) have shown a non-linearity equivalent to a 1 nm displacement. Equivalent results have been achieved from the runs taken where the eighth harmonic (360° phase change equivalent to about 20 nm) of the heterodyne signals was detected. Due to the use of un-buffered electronics in the high harmonic detection larger noise was observed from these runs. The problem has subsequently been solved.

Post-processing of data based on the normalization parameters (amplitudes and offsets of the *XY* components of the two phases) recorded before measurement runs has shown a reduction of the non-linearity of the voltage applied to the EOM down to about an equivalent 0.15 nm (figure 14). Nevertheless, components of the non-linearity are still visible in the graph of residuals. Some improvement in the compensation could be obtained with further refinements of data processing and the normalization procedure. In addition, some drift caused by the additional heat due to the electronics inside the box is also visible. Data were not corrected for changes of the material/optics temperature inside the box. Currently, data acquisition and control makes use of a multiplexed-channels board. The use of a parallel-type board is foreseen in the near future which would help eliminate crosstalk between data acquisition channels.

4.4. Separated beams heterodyne interferometer (PTB)

For the determination of the non-linearities, the lamella of the XRI was stepped through a distance of 288 nm or 1500 x-ray fringes. This displacement was equivalent to 2.2 optical

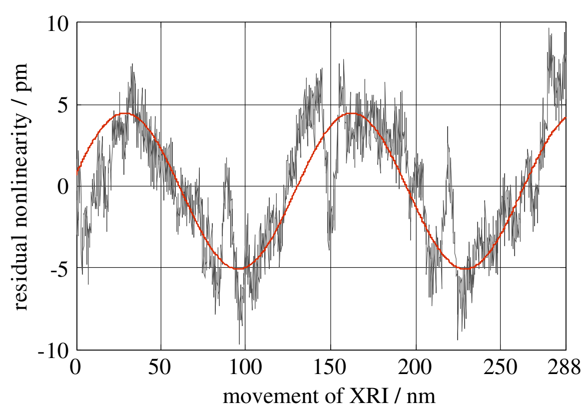

Figure 15. PTB interferometer residual non-linearities and best fit. Equation of best fit $Y_{\mathrm{NL}} = 0.3\,\mathrm{pm} + 4.78\,\mathrm{pm} \times (\sin(2\pi x/133.05\,\mathrm{nm}) + 0.21)$.

fringes of PTB's interferometer. After each step of the XRI, its position was stabilized and after a waiting time of 80 ms, a trigger started the acquisition of 5000 phase values from the optical interferometer with an acquisition rate of 48.8 kHz. The variation of the 5000 phase values is caused by the position deviations of the XRI, the noise of the optical interferometer and the drift of both systems. The standard deviation at each measurement point detected by the optical interferometer remained smaller than 11 pm, which is larger than the 8 pm measured when a common mirror was used for the measurement and reference beams. In addition these measurements over 5 min revealed that thermal drift of the optical interferometer was negligible compared with its noise. The measured position at each step represents an average over the 5000 phase values.

Based on the assumption of an error-free XRI, the non-linearities of the optical interferometer are determined by the deviations of the measured positions from a best-fit line. To emphasize the periodic non-linearities of the optical interferometer the measurement over 1500 XRI steps was repeated six times, three times forwards and three times backwards. The thermal stability of the combined optical and XRI enabled an average over six of the deviations from the best-fit lines. This average represents the time-independent non-linearity of the combined setup, which was smaller than ± 10 pm (grey curve in figure 15). A fitted sinusoidal wave with the periodicity of the optical interferometer exhibits an amplitude of 4.8 pm (red curve in figure 15).

4.5. Non-linearity correction using a capacitive sensor (MIKES)

The two photodetectors and the capacitive sensor of the MIKES setup had a built-in preamplifier circuit and produced some additional heat inside the box that caused drift in both the optical and the x-ray interferometers. Vibration and air turbulence noise in the interferometer signal was small, but the drift in the periodic non-linearity parameters was observed to be faster than in the previous setup (Seppä *et al* 2011), probably as a result of a slow temperature drift. After tuning the optics,

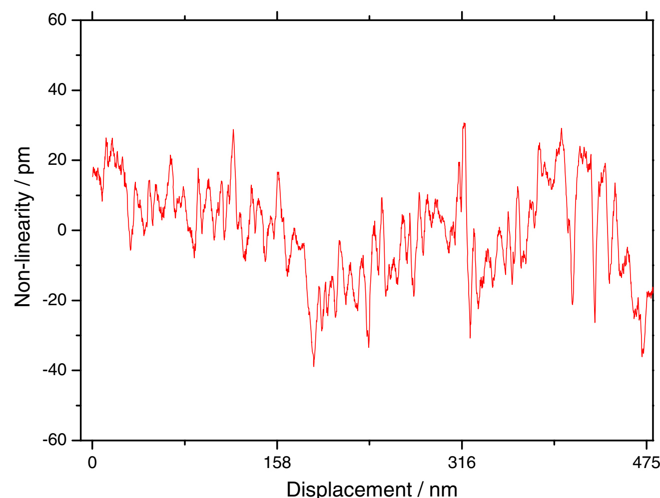

Figure 16. Residual non-linearity in the MIKES interferometer. Note a fitted line has been subtracted from the difference between the XRI and MIKES interferometer.

the amplitude of the uncorrected periodic non-linearity was approximately 300 pm.

Because the drift of the periodic non-linearity parameters was significant, measurement of the correction was carried out as fast as possible just before the actual comparison measurement scan. The duration of the determination of the periodic correction was roughly 15 min and the actual comparison scan with 4000 x-ray fringes took 12 min, giving a time difference of 10 min to 20 min between correction measurement and application.

During the linearization scan the piezo voltage of the XRI moving mirror was scanned without feedback from the x-ray detector and the MIKES interferometer system recorded synchronized interferometer and capacitive sensor readings, yielding a fresh periodic linearization function for the MIKES interferometer phase value. After the measurement of the periodic correction, the interferometer was used to record data whilst the XRI stepped through consecutive x-ray fringes. The signal from the MIKES interferometer was continuously recorded, and a simple algorithm was used to detect when the XRI changed position. One hundred samples were averaged 70 ms after each fringe jump. In figure 16 the data for approximately 2500 x-ray fringes are shown, filtered with a flat moving average window 16 x-ray fringes long. The validity of the periodic correction gradually deteriorates during the measurement due to drifts. The rms residual error for the data in the figure is 14 pm.

5. Conclusions and outlook

The work in the NANOTRACE project has shown that achieving displacements with sub-nanometre accuracy is a non-trivial task. All the systems developed within this project are complex and involve the use of combinations of intricate and sometimes custom manufactured optics, electronics and software. The comparisons with the x-ray interferometer provided valuable information on the performance of the optical interferometers and in some cases this comparison

has identified aspects of a particular design that needed improvement. For each comparison careful alignment of the interferometers with respect to the x-ray interferometer was required and initial measurements often showed that further alignment was necessary to minimize the non-linearity in the interferometer. The re-alignment was both to take into account any polarization leakage in the interferometer and also to minimize the effect of any stray reflections. This naturally presents a challenge when these interferometers are used to provide traceable measurements without an independent method for measurement of the non-linearity present in the interferometer. The comparison has shown that several methods are able to realize optical interferometers with non-linearity at the sub-10 pm level; however, the remaining challenges are to determine fully other sources of errors in the interferometers and to develop a system whose performance is reproducible in a variety of different settings.

Acknowledgments

The authors would like to thank their respective governments for funding as well as the European Commission for funding from the European Community's Seventh Framework Programme, ERA-NET Plus, under Grant Agreement No 217257. Gian Bartolo Picotto wishes to acknowledge the work of R Bellotti, A Giugni and M Santiano who designed the electronics, control software and mechanical assembly of the INRIM interferometer. Jeremias Seppä wishes to thank the Wihuri foundation for support. Andrew Yacoot thanks NPL Engineering Services for the design and construction of the platform for the x-ray interferometer and Nigel Cross for providing engineering support during the comparison measurements at NPL. © 2012 Crown copyright.

Disclaimer

The naming of any manufacturer or supplier by the authors in this paper shall not be taken to be endorsement of specific samples of products of the said manufacturer, or recommendation of the said supplier. Furthermore, the authors cannot be held responsible for the use of, or inability to use, any products mentioned herein that have been used by them.

References

Andreas B *et al* 2011 Determination of the Avogadro constant by counting atoms in a ^{28}Si crystal *Phys. Rev. Lett.* **106** 030801

Basile G *et al* 2000 Combined optical and x-ray interferometer for high precision dimensional metrology *Proc. R. Soc.* A **456** 701–29

Bergamin A, Cavagnero G and Mana G 1997 Quantized positioning of x-ray interferometers *Rev. Sci. Instrum.* **68** 17–22

Birch K P 1990 Optical fringe division with nanometric accuracy *Precis. Eng.* **12** 195–8

Bitou Y 2009 High-accuracy displacement metrology and control using a dual Fabry–Perot cavity with an optical frequency comb generator *Precis. Eng.* **33** 187–93

Bobroff N 1993 Recent advances in displacement measuring interferometry *Meas. Sci. Technol.* **4** 907–26

Bonse U and Hart M 1965a An x-ray interferometer *Appl. Phys. Lett.* **6** 155–6

Bonse U and Hart M 1965b Principles and design of Laue case x-ray interferometers *Z. Phys.* **88** 154–64

Budker D, Rochester S M and Yashchuk V V 2000 Obtaining frequency markers of variable separation with a spherical mirror Fabry–Perot interferometer *Rev. Sci. Instrum.* **71** 2984–7

Danzebrink H-U, Koenders L, Wilkening G, Yacoot A and Kunzmann H 2006 Advances in scanning force microscopy for dimensional metrology *Ann. CIRP* **55** 1

Durand M, Lawall J and Wang Y 2011 High-accuracy Fabry–Perot displacement interferometry using fiber lasers *Meas. Sci. Technol.* **22** 094025

Gamidov R, Çetintaş M, Sadıkhov E and Sautenkov V 1996 Diode laser with external optical feedback for small displacement measurements *Digest of Conf. on Precision Electromagnetic Measurements (Braunschweig, Germany)* pp 126–7

Haitjema H, Schellekens P H J and Wetzels S F C L 2000 Calibration of displacement sensors up to 300 µm with nanometre accuracy and direct traceability to a primary standard of length *Metrologia* **37** 25–33

Hart M 1968 Angstrom ruler *J. Phys. D: Appl. Phys.* **1** 1405–8

Heydemann P L M 1981 Determination and correction of quadrature fringe measurement errors in interferometers *Appl. Opt.* **20** 3382–4

Hou W M, Zhang Y B and Hu H J 2009 A simple technique for eliminating the nonlinearity of a heterodyne interferometer *Meas. Sci. Technol.* **20** 105303

ITRS 2009 *International Technology Roadmap for Semiconductors*

Korpelainen V, Seppä J and Lassila A 2010 Design and characterization of MIKES metrological atomic force microscope *Precis. Eng.* **34** 735–44

Křen P and Balling P 2009 Common path two-wavelength homodyne counting interferometer development *Meas. Sci. Technol.* **20** 084009

Kruk P, Noga A, Trepka T, Zachorowski J and Gawlik W 2005 Frequency reference for laser spectroscopy with the stabilized 4-m-long Fabry–Perot cavity *Rev. Sci. Instrum.* **76** 033109

Lawall J and Kessler E 2000 Michelson interferometry with 10 pm accuracy *Rev. Sci. Instrum.* **71** 2669

Lawall J R 2005 Fabry–Perot metrology for displacements up to 50 mm *J. Opt. Soc. Am.* A **22** 2786–98

Leach R K *et al* 2011 The European Nanometrology Landscape *Nanometrology* **22** 062001

Martin J, Kuetgens U, Stümpel J and Becker P 1998 The silicon lattice parameter—an invariant quantity of nature? *Metrologia* **35** 811–7

Massa E, Mana G, Kuetgens U and Ferroglio L 2009 Measurement of the lattice parameter of a silicon crystal *New J. Phys.* **11** 053013

Mohr P J, Taylor B N and Newell D B 2008 CODATA recommended values of the fundamental physical constants: 2006 *Rev. Mod. Phys.* **80** 633–730

Nerino R, Sosso A and Picotto G B 1997 A novel ac current source for capacitance-based displacement measurements *IEEE Trans. Instrum. Meas.* **46** 640–3

Peggs G and Yacoot A 2002 A review of recent work in sub-nanometre displacement measurement using optical and x-ray interferometry *Phil. Trans. R. Soc.* **360** 953–68

Quinn T J 2003 Practical realization of the definition of the metre, including recommended radiations of other optical frequency standards (2001) *Metrologia* **40** 103–33

Roos P A, Stephens M and Wiemann C E 1996 Laser vibrometer based on optical-feedback-induced frequency modulation of a single-mode laser diode *Appl. Opt.* **35** 6754–61

Seppä J, Korpelainen V, Merimaa M, Picotto G B and Lassila A 2011 A method for linearization of laser interferometer down

to picometre level with a capacitive sensor *Meas. Sci. Technol.* **22** 094027
SIS3302, Struck Innovative Systeme, Hamburg, information available at http://www.struck.de/sis3302.htm (accessed 22 November 2011)
Stone J A, Decker J E, Gill P, Juncar P, Lewis A, Rovera G D and Viliesid M 2009 Advice from the CCL on the use of unstabilized lasers as standards of wavelength: the helium–neon laser at 633 nm *Metrologia* **46** 11–18
Tanaka M, Yamagami T and Nakayama K 1989 Linear interpolation of periodic error in a heterodyne laser interferometer at subnanometer levels *IEEE Trans. Instrum. Meas.* **38** 552
Windisch D and Becker P 1990 Silicon lattice parameters as an absolute scale of length for high precision measurements of fundamental constants *Phys. Status Solidi* a **118** 379–88
Yacoot A and Cross N R 2003 Measurement of picometre non-linearity in an optical interferometer grating encoder using x-ray interferometry *Meas. Sci. Technol.* **14** 148–52
Yacoot A and Downs M J 2000 The use of x-ray interferometry to investigate the linearity of the NPL differential plane mirror optical interferometer *Meas. Sci. Technol.* **11** 1126–30
Yacoot A, Koenders L and Wolff H 2007 An atomic force microscope for the study of the effects of tip–sample interactions on dimensional metrology *Meas. Sci. Technol.* **18** 350–9
Yacoot A and Kuetgens U 2012 Sub-atomic dimensional metrology: developments in the control of x-ray interferometers *Meas. Sci. Technol.* **23** 074003